remote sensing

MDPI

Article

Infrasound and Low-Audible Acoustic Detections from a Long-Term Microphone Array Deployment in Oklahoma

Trevor C. Wilson, Christopher E. Petrin and Brian R. Elbing *

School of Mechanical & Aerospace Engineering, Oklahoma State University, Stillwater, OK 74078, USA
* Correspondence: elbing@okstate.edu

Abstract: A three-microphone acoustic array (OSU1), with microphones that have a flat response from 0.1 to 200 Hz, was deployed for 6 years (2016–2022) at Oklahoma State University (OSU) in Stillwater, Oklahoma, and sampled at 1000 Hz. This study presents a new dataset of acoustic measurements in a high interest region (e.g., study of tornado infrasound), provides a broad overview of acoustic detections and the means to identify them, and provides access to these recordings to the broader scientific community. A wide variety of infrasound and low-audible sources were identified and characterized via analysis of time traces, power spectral densities, spectrograms, and beamforming. Low, median, and high noise models were compared with global noise models. Detected sources investigated include natural (microbaroms, bolides, earthquakes, and tornadoes) and anthropomorphic (fireworks, airplanes, and munition detonations) phenomena. Microbarom detections showed consistency with literature (~0.2 Hz with peak amplitude in the winter) and evidence that the frequency was inversely related to the amplitude. Fireworks and airplanes served as verified local events for the evaluation of data quality and processing procedures. Infrasound from munition detonations, that occur nearly daily at a location 180 km southeast of OSU1, matched the available ground truth on days with favorable propagation to OSU1. A clear bolide detection with an estimated position of approximately 300 km from OSU1 was shown. Most detected earthquakes were seismic arrivals due to sensor vibrations; however, the largest earthquake in Oklahoma history showed an acoustic arrival. Finally, data from multiple tornadoes are discussed, including a previously unpublished quasi-linear convective system tornado.

Keywords: infrasound; tornadoes; earthquakes; bolide; microbaroms; noise model; sensor array

Citation: Wilson, T.C.; Petrin, C.E.; Elbing, B.R. Infrasound and Low-Audible Acoustic Detections from a Long-Term Microphone Array Deployment in Oklahoma. *Remote Sens.* **2023**, *15*, 1455. https://doi.org/10.3390/rs15051455

Academic Editors: Alain Hauchecorne, Constantino Listowski and Patrick Hupe

Received: 14 December 2022
Revised: 28 February 2023
Accepted: 2 March 2023
Published: 5 March 2023

1. Introduction

The atmospheric conditions within the state of Oklahoma are known as some of the most widely monitored in the world due to Oklahoma's diverse weather patterns and propensity for producing some of the largest tornadoes. For this reason, Oklahoma was originally selected as the location for the United States (US) National Weather Service (NWS) Storm Prediction Center (SPC). The SPC is responsible for monitoring and categorizing severe storms and events (e.g., hail and tornadoes) for the contiguous US. Other long-term monitoring efforts in Oklahoma include an Atmospheric Radiation Measurement (ARM) site, the Oklahoma Mesonet [1], and the Advanced Radar Research Center (ARRC). The Southern Great Plains (SGP) ARM site is one of three worldwide ARM monitoring sites. The SGP-ARM observatory is the world's largest and most extensive climate research facility, which includes radiometers, radars, LIDARs, sky imager, and radiosondes. The Oklahoma Mesonet consists of 120 automated ground stations covering the entire state that measure air and soil temperature, relative humidity, wind speed and direction, barometric pressure, rainfall, and incoming solar radiation. Due, in part, to these resources, Oklahoma is a frequent location for atmospheric field campaigns. Recent campaigns include the 2003 Oklahoma City Joint Urban field campaign [2], 2017 Land-Atmosphere

Feedback Experiment [3], 2019–2021 pilot aerosol microphysics network [4], the Collaboration Leading Operational UAS Development for Meteorology and Atmospheric Physics (CLOUD-MAP) [5–8], and the Weather Intelligent Navigation Data and Models for Aviation Planning (WINDMAP) [9]. In addition, this makes Oklahoma a good candidate for atmospheric infrasound (i.e., sound at frequencies below human hearing) studies, since infrasound propagation is sensitive to the atmospheric conditions. Consequently, there are several studies (past and present) in Oklahoma related to atmospheric infrasound propagation from severe storms [10–12], munition detonations [13,14], and earthquakes [15–17]. An understanding of the background noise levels and common sources (e.g., microbaroms) is extremely valuable in the analysis of data for these studies. Most of these phenomena produce sound in the near-infrasound range of 0.1 Hz to the low-audible range (~40 Hz). Therefore, the current work reports on a long-term (~6 years) deployment of an infrasound and low-audible array in Oklahoma to characterize background infrasound levels and identify several sources (e.g., microbaroms, explosions, and tornadoes).

Arrays are used to investigate complex wavefields, including acoustic, seismic, and astronomic [18]. Arrays are preferred over single sensors for these studies since they provide enhanced signal detection in the presence of noise (e.g., wind). This is due to the fact that the summation effect increases the Signal-to-Noise Ratio (SNR) as a result of the presence of multiple measurements with varying incoherent noise. In addition, arrays can provide an estimation of the signal directionality [19,20], which typically requires a minimum of three sensors. Arrays are widely used in studying infrasound-producing sources, including earthquakes [21], lightning [22], meteors [23], explosions [24], interacting ocean waves [25], avalanches [26], volcanoes [27], and tornadoes [10,11]. The ability for an array to detect a source depends on its spatial layout, sample rate, the spectral content of source, propagation conditions, and local background noise levels. While most array processing techniques require at least three array elements, more array elements generally provide improved performance (e.g., back azimuth accuracy, higher SNR). The lowest frequency an array can beamform is set by the array aperture, the largest distance between two elements.

The International Monitoring System (IMS) was created for treaty verification as part of the Comprehensive Nuclear-Test-Ban Treaty (CTBT) [28]. The IMS network consists of over 300 seismic, infrasound, hydroacoustic, and radionuclide monitoring facilities across the globe. The goal of infrasound monitoring in this treaty is to detect atmospheric nuclear tests, though in some specific cases, infrasound sensors have detected underground nuclear tests [29,30]. The current atmospheric infrasound study focuses on regional monitoring with a relatively high sample frequency (1000 Hz) with sensors that have a nearly flat response from 0.1 Hz to the low-audible range (200 Hz). The sample rate was set higher than the upper bound of the flat response to avoid resolution limitations when computing the time-difference-of-arrival. This expands the range of detectable events to higher frequencies as well as decreases the impact of temporal resolution on beamforming precision. The three-microphone array (OSU1) was deployed at Oklahoma State University (OSU) from 2016 to 2022. All data from this article are publicly available [31], and any additional data are available upon reasonable request. The data (pressure time traces) for each channel (i.e., microphone) are stored in Seismic Analysis Code (SAC) file format. The goal of this study is to present this new dataset to the broader scientific community, including the analysis of specific examples. The remainder of the paper includes the study methodology for the collection and analysis of the infrasound data in Section 2, characterization of the ambient noise in Section 3.1, identification of a wide variety of infrasound producing sources (e.g., microbaroms, fireworks, airplanes, munition explosions, bolides, earthquakes, and tornadoes) in Section 3.2, discussion of the results and potential use of this database in Section 4, and conclusions drawn in Section 5.

2. Materials and Methods

2.1. Infrasound Array

2.1.1. Layout and Sensors

A single infrasound microphone (OSU1-W) on the north side of the OSU campus began recording on 2 September 2016. In January 2017, this was expanded to a three-microphone (Model 24, Chaparral Physics) array termed OSU1 and was operational for 6 years. The original deployment was for CLOUD-MAP [5–8], a multi-university collaboration focused on the development and implementation of Unmanned Aerial Systems (UAS) and their integration with atmospheric sensors, but has subsequently been used for several other projects. An illustrated satellite image of the array is provided in Figure 1. It was centered at (36.1344°, −97.0815°) with the coordinates for each sensor listed in Table 1 along with the separation distances between other sensors. The height difference between the roof and ground microphones was as high as 6 m, which creates a maximum of 6° angle relative to horizontal. The separation distances listed in Table 1 are horizontal distances that require correction if inclination angles are being resolved. In the current study, inclination angles are accounted for based on the range of acceptable trace velocities, in which this angle creates less than a 1% uncertainty in the trace velocity. Given that the maximum wavelength that can be directionally resolved using traditional beamforming techniques is nominally twice the sensor spacing, the current array with an average sensor spacing of 62 m can readily detect sources using traditional methods down to 2.8 Hz. Each microphone had a nominal sensitivity of 400 mV/Pa and a frequency response that was flat (0 to −3 dB) from 0.1 to 200 Hz.

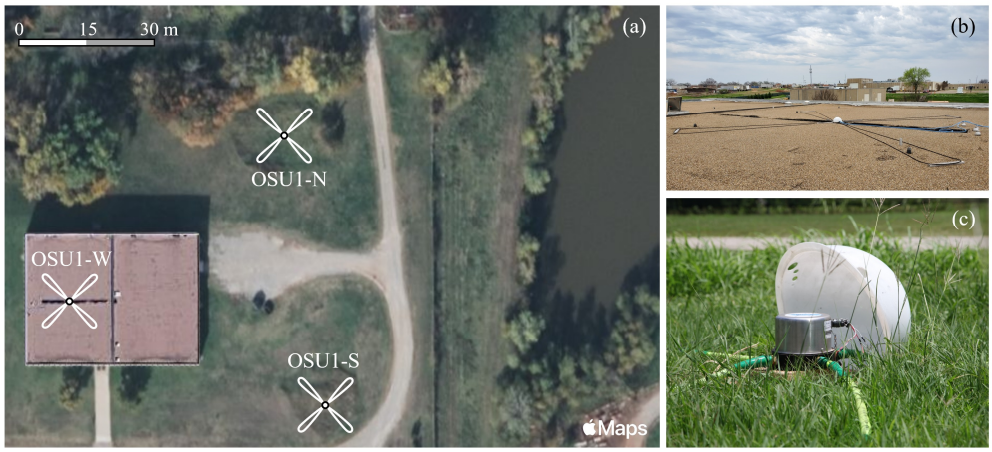

Figure 1. (**a**) Satellite image of the OSU1 infrasound array with each microphone labelled and denoted by the white X-pattern, which nominally marks the porous hose windscreen configurations (Source: Apple Maps). (**b**) Picture of OSU1-W mounted within the white acrylic dome and porous hoses extending from the sensor. (**c**) Picture of OSU1-S with the dome opened to show the sensor.

Table 1. Summary of microphone locations (including elevation, *z*), mounting location (roof or ground), and the separation distance between the microphones.

	Location				Separation Distance (m)		
	Lat (°)	**Lon (°)**	***z* (m)**	**Mount**	**OSU1-W**	**OSU1-N**	**OSU1-S**
OSU1-W	36.1344	−97.0819	296	Roof	0	67.6	58.6
OSU1-N	36.1342	−97.0813	291	Ground	67.6	0	58.5
OSU1-S	36.1347	−97.0814	290	Ground	58.6	58.5	0

Each microphone was mounted on a low-frequency vibration isolation pad and housed within an acrylic dome painted in white (see Figure 1b,c) to mitigate the impact of rapid temperature variations. Spatial filtering windscreens in the "X" pattern shown in Figure 1

were formed with four 15-m long, 9.5 mm diameter rubber porous hoses (CELSP38050 SoakerPro, Swan, Sandy Springs, GA, USA) connected to each microphone. The microphones with and without the windscreens (hoses) were tested in an anechoic chamber (though not anechoic to infrasound frequencies) in a method similar to Hart and McDonald [32]. These results showed broadband wind noise reduction with an average of 7.8 dB reduction for wind speeds below 4.7 m/s with signal attenuation for frequencies above 50 Hz [33]. The microphones were powered with DC-power supplies (APS-1303, Aktakom, Miami, FL, USA) with the output recorded via a dynamic signal analyzer (USB-4432, National Instruments, Austin, TX, USA). The data acquisition was controlled via a commercial software package (Sound and Vibration Measurement Suite, National Instruments, Austin, TX, USA). The sample rate was fixed at 1000 Hz and typically grouped in 20-min observation windows.

2.1.2. Calibration

The noise floor for each OSU1 sensor is compared with global low and high background levels [34,35] in Figure 2, which shows that the electrical noise of these sensors was below the global low background levels for frequencies below ~3 Hz. OSU1-S was replaced in March 2021, due to a blown amplifier. An in situ calibration was performed on the array in May 2018. A 12.7 mm (0.5 in.) pressure microphone (Type 40AD, GRAS Sound & Vibration, Holte, Denmark) with a CCP preamplifier (Type 26 CA, GRAS) was calibrated onsite with a pistonphone (42AB, GRAS) at 1000 Hz. Then, the 12.7 mm (0.5 in.) microphone was co-located with a given array microphone, while a 153 Hz tone was played. This calibration showed less than 2% deviation from the manufacturer supplied calibration. Since this calibration was limited to higher (audible) frequencies, the three sensors were calibrated against each other using common long-range sources. Microbaroms, as discussed further subsequently, are a common 0.2 Hz source that can propagate over thousands of kilometers, which the amplitude variation between the three sensors separated by ~60 m should be minimal. This showed that OSU1-W consistently had the largest amplitude with OSU1-S and OSU1-N having ~10% lower amplitude. Due to the layout of the array relative to the data acquisition, OSU1-W had a significantly shorter cable length. Consequently, the other microphones were calibrated to OSU1-W with factors of 1.011 and 1.095 applied to OSU1-S and OSU1-N, respectively. The resulting average power spectra when microbaroms were detected (not shown) show an excellent agreement between microphones, especially between OSU1-W and OSU1-N between 2 and 20 Hz. However, OSU1-S was consistently lower in amplitude between 1 and 20 Hz with the maximum deviation being ~4 dB. Moreover, this was repeated with a bolide detection as reported subsequently and showed similar results.

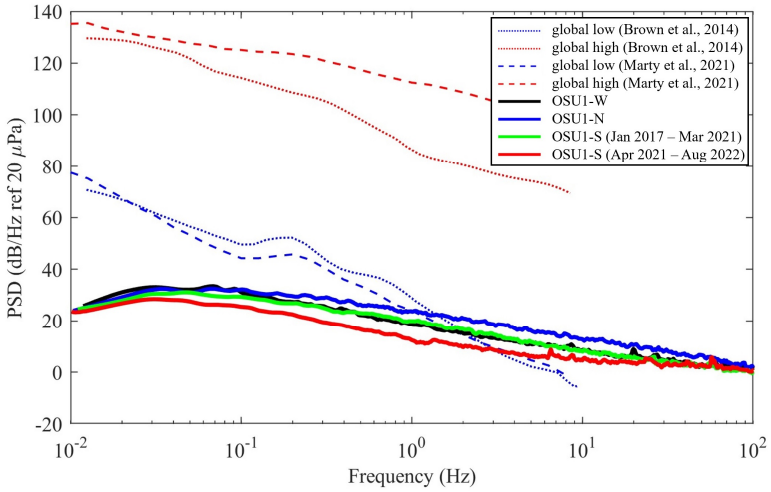

Figure 2. OSU1 microphone noise floors compared with low and high global noise levels [34,35].

2.1.3. Array Response

Spatial aliasing of an array is commonly quantified by displaying its array response on a slowness grid $\vec{p} = (p_x, p_y)$, which conveys information about the apparent sound speed (c_{app}). The apparent sound speed accounts for the inclination angle (θ) of the propagating wave relative to the horizontal (i.e., when $\theta = 0$ the wave propagates horizontally) such that $c_{app} = c_{eff}/\cos\theta$, where the effective sound speed c_{eff} is defined as follows:

$$c_{eff} = \sqrt{\gamma RT} + \hat{n}_{xy} \cdot \vec{u} \, . \tag{1}$$

Here γ is the heat capacity ratio (1.4 for air); R is the specific gas constant (287.05 J/kg·K for air); T is the absolute temperature; $\hat{n}_{xy}$ is the direction from the source to the receiver; and $\vec{u}$ is the wind vector. The magnitude of the slowness grid equals the inverse of c_{app} with $p_x = \left|\vec{p}\right| \cos\phi$ and $p_y = \left|\vec{p}\right| \sin\phi$ for all possible back azimuth (BAZ) angles (ϕ), in which ϕ is measured clockwise from the north and is the direction of a wave traveling toward an observer (i.e., $\phi = 270°$ is a wave traveling from west to east). The beamforming array response pattern is derived from the Frequency-Wavenumber (FK) spectrum analysis assuming a planar wave [36], and is referred to as the array beampattern, the array transfer function, or the spatial window function [37,38]. The resulting array response for OSU1 at frequencies of 3, 8, and 20 Hz is provided in Figure 3. For reference, concentric circles corresponding to sound speeds of 420, 343, and 320 m/s are included from the inner to the outer circle. These can be considered respectively to correspond with a 35° inclination angle with no opposing wind speed, 0° inclination angle with no opposing wind speed, and 0° inclination angle with 23 m/s of opposing wind speed.

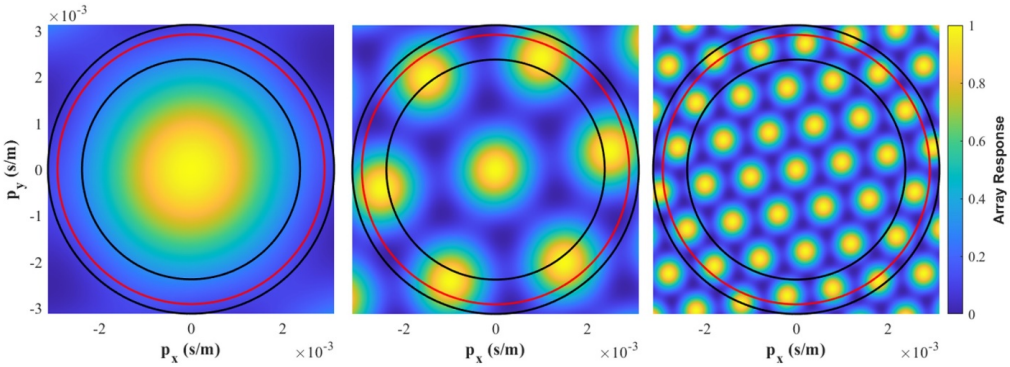

Figure 3. Beamforming array response for OSU1 at (**left**) 3 Hz, (**middle**) 8 Hz, and (**right**) 20 Hz. The three concentric circles correspond to 420, 343, and 320 m/s (from the inner to the outer circle).

For each frequency, there is a main lobe (i.e., bright spot) at the origin, $(p_x, p_y) = (0, 0)$, which its diameter increases with decreasing frequency. At a given frequency, the main lobe diameter is set by the array aperture, which would be ~60 m for OSU1. For the current array, the main lobe diameter for 0.2 Hz is larger than the acoustic sound speed, which means that OSU1 cannot accurately resolve the direction of arrival with traditional beamforming for microbaroms, even though it can measure signals at that frequency. Additional lobes (i.e., bright spots) are present for 8 and 20 Hz in Figure 3. These are known as side lobes and cause spatial aliasing as a result of the array's design (aperture, sensor count, and layout). OSU1 only had three elements, and thus they were positioned in nearly an equilateral triangle to mitigate the impact of side lobes. However, for frequencies above ~3 Hz, the side lobes have an impact on the array's accuracy in resolving the direction of arrival, which can be nominally quantified by the number and magnitude of lobes inside the concentric circles.

2.1.4. Operation

As previously stated, OSU1-W began recording on 2 September 2016 and the other two microphones began in January 2017. Figure 4 provides a full timeline of the recording from OSU1 with the bar graph for each year showing the percentage of the day recorded. Gaps in the recording were primarily the product of damage to the array, maintenance, or the data acquisition system crashing. Some examples of array damage include a backhoe pulling out the cables and an animal repeatedly chewing through the OSU1-S cables. Maintenance efforts included replacing cables and connectors as well as inspecting the performance of the microphones. Finally, the data acquisition system would sporadically crash with the periods in between crashes ranging from days to months. Since this array was originally built to monitor tornadoes, OSU1 was closely monitored during the Oklahoma tornado season (April–June) to resolve any issues rapidly.

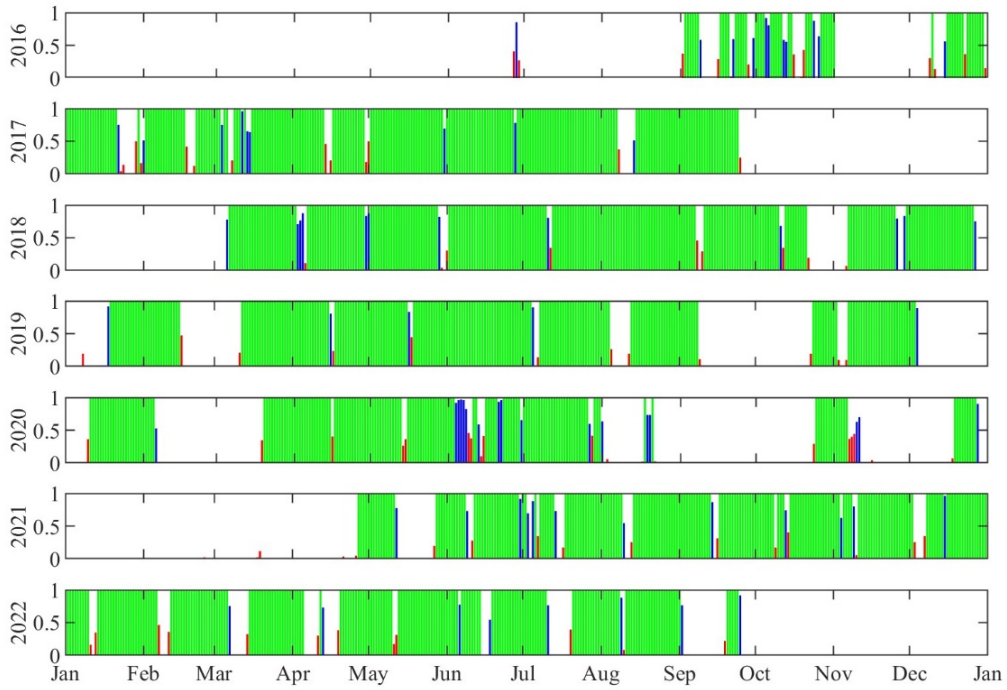

Figure 4. Timeline highlighting data availability for OSU1, the array began recording in September 2016 and was decommissioned in September 2022. Bars indicate the percentage of the day recorded. Bars are colored (green) for 100%, (blue) for >50%, and (red) for <50% of data availability for the day. Blank areas indicate that the array was not recording data.

2.2. Ground Conditions

A limitation of the OSU1 deployment was the lack of a local weather station. For a portion of the OSU1 deployment, there was a weather station (Vantage Pro, Davis Instruments) located 170 m south of OSU1 that recorded 30-min average temperature, humidity, atmospheric pressure, and wind speed. However, the data had to be specially requested from the operators and the station was permanently damaged by lightning in 2020. While further away from OSU1, a more consistent and reliable source of local weather conditions is the Stillwater (STIL) Oklahoma Mesonet station [1,39]. The Oklahoma Mesonet network consists of 120 automated environmental monitoring stations that measure air temperature 1.5 m above ground, relative humidity 1.5 m above ground, wind speed and direction 10 m above ground, barometric pressure, rainfall, incoming solar radiation, and soil temperature. The STIL station also provides measurements of the air temperature 9 m above ground and wind speed 2 m above ground. The data are publicly available through several methods and sites (e.g., mesonet.org, accessed on 2 March 2023). Data are packaged in 5-min "observations" that are quality checked by the Oklahoma Climatological Survey

prior to being released. The subsequent assessment of OSU1 under various wind conditions uses the Mesonet data only since that is publicly available to other researchers.

2.3. Signal Processing

In the current work, OSU1 data have been presented as pressure time traces, power spectral densities, spectrograms, and variations on beamforming techniques. For spectral content frequency band, the window size and percentage overlap varied depending on the source being investigated. The sound pressure spectra $\Phi(f)$ were computed in the single-sided form as follows:

$$P_{rms}^2 = \int_0^\infty \Phi(f) df, \tag{2}$$

where P_{rms}^2 is the pressure variance and f is the temporal frequency. The computation of the power spectral density was carried out using the Welch method [40], with the window size and overlap selected based on the source of interest. The temporal variation of spectral content was commonly assessed using spectrograms. The spectrograms were computed using the short-time Fourier transforms with control over the window size and overlap. While custom beamforming algorithms were created, most of the presented work leverages established toolkits. ObsPy [41,42] is an open source Python based package developed as a framework for viewing and processing seismological data. Moreover, Obspy can be used for infrasonic data due to similarities in data formats, filtering, instrumentation correction, and data visualization. Furthermore, ObsPy offers a direct methodology for obtaining open-access waveforms and station metadata from databases, such as the Incorporated Research Institutions for Seismology (IRIS). This is valuable as the IRIS database has several stations that record infrasound, which can be compared when examining long range propagation. InfraPy [43] is an infrasound specific analysis toolkit developed at Los Alamos National Lab. Specifically, InfraPy was designed to apply detection, association, localization, and characterization algorithms for the investigation of ground-based nuclear detonations. Due to the fact that the OSU network consists of a singular array, only the array analysis tools (detection algorithms) were utilized in this study. A more advanced array signal processing technique termed the Cardinal Detector [44] was recently developed. This is an automated processing algorithm that augments the default ObsPy FK analysis with the Progressive Multi-Channel Correlation (PMCC) algorithm [45]. FK analysis is an array processing technique that allows for the calculation of a back azimuth, apparent velocity, and coherence of a signal arriving at an array [46]. The application of PMCC to the standard FK processing allows for the analysis of multiple frequency bands at the same time using a varying time window for overlapping frequency bands. The time windows are optimized for the signal band of interest and provide the ability to more accurately distinguish between signals of varying frequency arriving across the array at the same time.

3. Results

3.1. Ambient Noise

3.1.1. Noise Model

A station noise model is a critical component in the evaluation of the data quality and is a useful tool in estimating the detectability of signals at specific frequencies and amplitudes [34,47]. Using the history of ambient noise (i.e., energy not associated with a source of interest) at a specific station, its noise model can be readily defined based on the Probability Distribution Function (PDF) of the Power Spectral Density (PSD) over a defined period of interest. The PDF was formed from 1-h average PSDs for every hour that OSU1 was operational. Each average PSD was produced using the Welch method [40] with 100 s windows and 50% overlap. Then, the OSU1 low and high noise models were defined as the 5th and 95th percentiles of the PDF, respectively. The resulting low, median, and high noise models for OSU1 are provided in Figure 5. These noise models are valuable for the automated assessment of data quality. However, the use of the noise model at higher frequencies should be carried out with caution as the 1-h period would produce a

poor representation of the PDF at these frequencies. The OSU1 noise model is compared against the global low and high noise models of Brown et al. [34] and Marty et al. [35]. Marty et al. [35] is a recently updated global model, but we have included Brown et al. [34] since the OSU1 noise model was produced in a similar fashion. This comparison shows that the upper noise levels observed at OSU1 were comparable to Brown et al. [34], but below Marty et al. [35], which is expected since Marty et al. [35] notes that their upper limit is primarily impacted by a single station in Antarctica. The OSU1 low noise model is elevated relative to the global averages. There are several likely reasons for the elevated low-noise model for OSU1, including time of day, time of year, and local conditions. The global noise models [34] were determined from sampling at predetermined times of the day (nominally 6 h between samples), while the OSU1 model was produced using all of the available 1-h periods. The second potential source (i.e., time of year) will create a bias error since this array primarily targeted severe weather, which resulted in being rarely nonoperational during the stormiest (and thus windiest) portions of the year (see Figure 4). Therefore, the noise model would have a sample bias toward these windier days in a region that is known for strong winds. The final potential reason was that the array was in close proximity to Stillwater, Oklahoma, a town of ~50,000 people in addition to the main campus of OSU. The increased human activity likely resulted in a significant elevation in the ambient noise, especially at higher frequencies. These potential issues were further investigated by examining the dependence on local wind speed, as well as identifying the spectral content from local sources, which are not of interest.

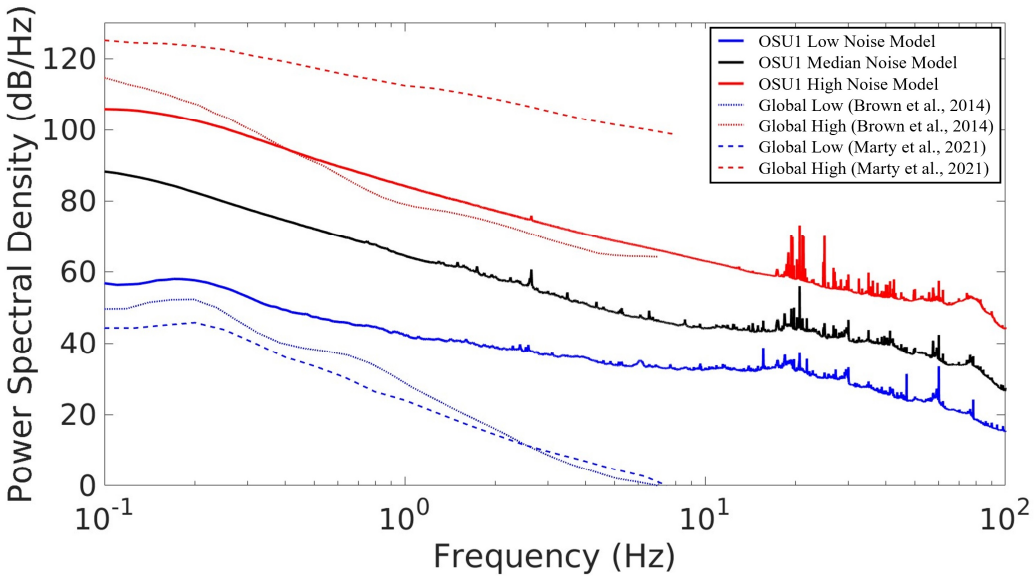

Figure 5. Power spectral density plot showing the OSU1 noise models (low, median, and high). These noise models are compared with the established global low and high noise models [34,35].

3.1.2. Wind Speed Dependence

Local winds have a significant impact on infrasound measurements, even with the use of windscreens. The OSU1 array used porous hoses as the windscreens. Pepyne and Klaiber [48] showed that porous hoses are effective windscreens at speeds above ~5 m/s. To investigate the noise model dependence on wind speed, the corresponding wind speed measured from the STIL Mesonet site [1,39] was stored with the 1-h average PSD. Then, the PSDs were sorted into 1 m/s bins, and the mean PSDs from the PDF for each wind speed for OSU1-N are plotted in Figure 6. Moreover, for reference, the global high and low noise models are included in Figure 6 [34,35], as well as a curve for a strong local source that will be discussed subsequently. These results show a steady rise in spectral levels with increasing speed for frequencies above ~0.2 Hz. The nominal trend is an increase of 1–1.5 dB/Hz per 1 m/s in wind speed, though there is an apparent frequency dependence

in this behavior (i.e., difference in separation between lines at 1 Hz versus 2 Hz). Moreover, there is a wind direction dependence due to the variations around each sensor, including topology, buildings, and natural wind breaks (e.g., trees). In general, OSU1 observed higher spectral content when the wind was from the south. This is not surprising since a row of trees exists directly to the north of OSU1, as seen in Figure 1, which would act as a windbreak when the wind was from the north. Here, it is important to reiterate that wind speed was not measured at OSU1 and the wind speed estimates are from a local Mesonet site that was 1.9 km southwest (219° back azimuth) of OSU1.

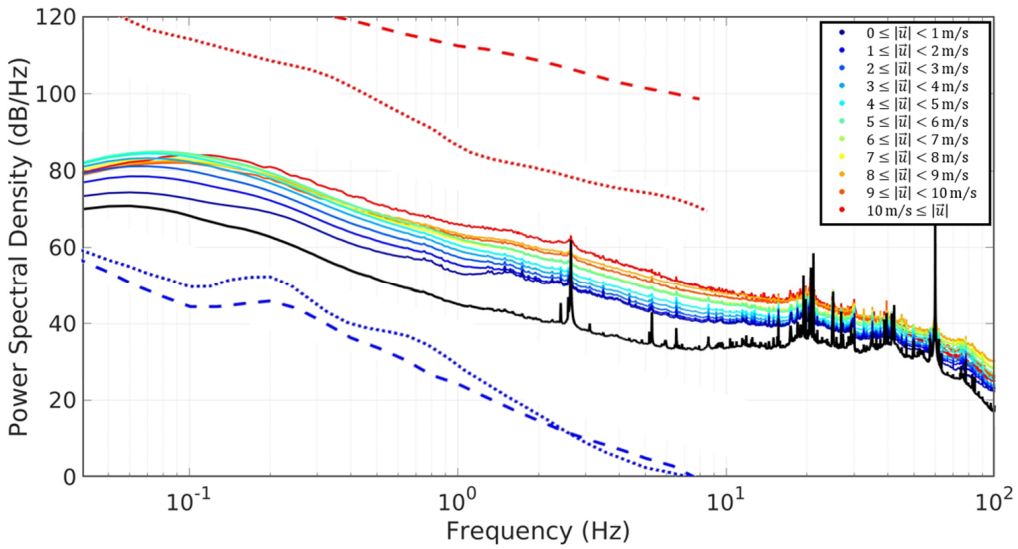

Figure 6. Mean spectra binned based on the average wind speeds measured by a nearby Mesonet site. The global low and high noise models [34,35] are included for reference. The thick black curve is the average of times when a recurring local noise source was present.

3.1.3. Semi-Regular Local Noise Sources

Here, we define local noise sources as semi-regular sources that are not of interest for detection or monitoring, and are sufficiently close that the plane wave assumption is not valid. A frequent source is a Fractionation Research facility that is ~150 m directly to the west of OSU1. This facility is intermittently operational with varying processes, which results in changes in the acoustic production. This makes it difficult to isolate its contributions, but the most frequent event is from a jet created by the venting of pressurized air. A spectrogram from a period of time when the jet was confirmed to be present showed a steady noise in the 12.5–25 Hz band. This suggests that the elevated spectral peaks in the noise models (Figure 5) above ~13 Hz are from this fractionation site since they are sufficiently regular to appear in the PDF of the PSDs.

Another recurring local noise source was identified when examining the wind speed dependence of the PSD (Figure 6). At each wind speed, there were noticeable irregular spectral peaks above ~1 Hz, which were observed on all three OSU1 sensors. Inspection of the individual 1-h PSD used to produce the mean spectra in Figure 6 revealed that these peaks were formed from a small number of high amplitude events. Consequently, a search for these events was performed and the resulting average is included in Figure 6. This spectrum has a very strong (66 dB) 2.6 Hz tone, a significantly weaker first harmonic (5.2 Hz), and elevated spectral content in the range consistent with the fractionation venting jet. There was a strong temporal variation of this signal with its occurrence primarily in the evening hours (i.e., between 8:00 pm and 8:00 am local time) and during the months of April, May, and June. Beamforming of the signal indicates a back azimuth of nominally 200°, but the resulting trace velocity is lower than physically possible. It is conjectured that the source was sufficiently close to the array that the plane wave assumption was invalid. This, combined with the elevated levels in the band known to be associated with

the fractionation site jet, suggests that it could also be from this site, even though the back azimuth angle should be ~265°. Regardless, any researchers leveraging this dataset should use caution in their analysis if the signal of interest is close to 2.6 Hz.

3.2. Examples of Event Detections

3.2.1. Microbaroms

Microbaroms are low frequency sounds (~0.2 Hz) observed all across the globe that were first reported in 1939 [49]. These signals are produced by a second-order non-linear interaction of ocean waves [50] of equal frequency but opposite propagation direction. Microbarom signals can propagate thousands of kilometers with the use of atmospheric wave-guides [51,52]. This makes microbaroms a regular reference signal used to assess the quality of data (e.g., [53]), and consequently microbaroms are the first source analyzed with OSU1. Here, it is important to note that microbarom signals are not always present since they rely on favorable atmospheric wave-guides. Therefore, a search for persistent high amplitude peaks in the microbarom frequency range (~0.2 Hz) was performed to locate potential detections. Over 1000 one-hour PSD averages were identified with a strong microbarom signal present. Each 1-h PSD was grouped based on the local wind speed recorded at the nearby Mesonet site to make the histogram in Figure 7. This shows that microbarom detections occurred primarily when wind speeds were below 5 m/s, which is consistent with the windscreen design being most effective below 5 m/s. This suggests that using the publicly available Mesonet database to identify low-wind periods is a robust means of filtering for low-noise data when searching for a given event. This was initially carried out for the current study to assess the quiescent ambient noise, but the reported noise models were not pre-filtered based on microbarom detections to avoid biasing the results.

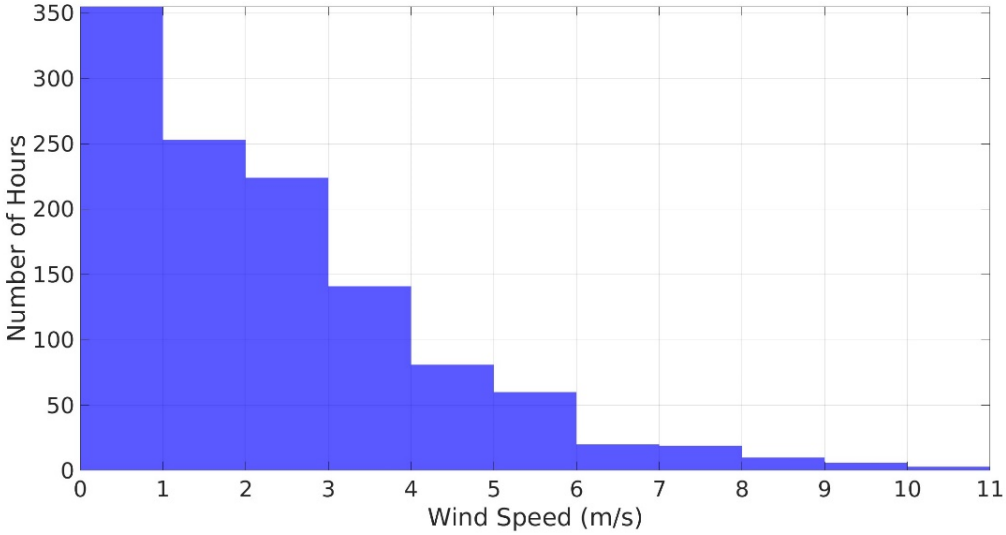

Figure 7. Histogram of microbarom detections as a function of wind speed measured at the nearby Mesonet station.

The microbarom amplitude has been shown to vary depending on the season [54,55] with the highest in the winter and lowest in the summer (for the northern hemisphere). For the current study, the microbarom-detected PSDs were computed for the Winter (December–February), Spring (March–May), Summer (June–August), and Fall (September–November) seasons and plotted in Figure 8. These results were consistent with the literature that showed significantly higher peaks during the winter, the lowest amplitude during the summer, and similar intermediate amplitudes for the spring and fall seasons. The higher amplitudes are due to the presence of large storms over the ocean [47] as well as a lower and stronger stratospheric waveguide [56,57], which aids in the propagation and reduces the attenuation

of microbarom signals. The peak microbarom amplitudes are denoted by star markers in Figure 8, which revealed the appearance of a weak empirical relationship between the amplitude (or season) and the peak frequency. As the amplitude increases, the microbarom frequency shifts to lower frequencies.

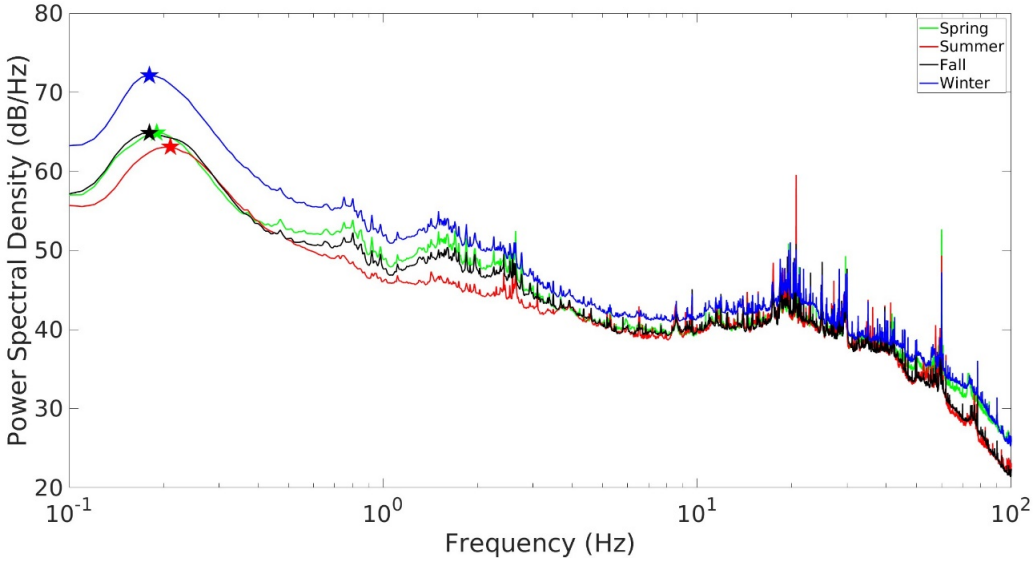

Figure 8. Average PSD with strong microbarom detection per season (Spring: March–May; Summer: June–August; Fall: September–November; Winter: December–February), with the peak microbarom amplitude marked with star markers.

3.2.2. Fireworks

Most years the city of Stillwater has a firework display 2–3 km to the northeast of OSU1 (the exact position varies year to year), which serves as a good reference source to test beamforming techniques and its ability to isolate multiple individual bursts. Each burst would produce a broadband signal from the low audible range (~200 Hz) down to nominally 1 Hz. FK analysis results from the 4 July 2018 firework show using a 4–15 Hz bandpass filter, 2 s windows, and 75% overlap are shown in Figure 9. In Figure 9, data points are closed (colored red) when the F-value, a measure of the signal-to-noise (SNR) ratio, exceeds a value of five, which was arbitrarily set to denote elevated coherence between microphones. These coherent periods have a relatively stable trace velocity at nominally 325 m/s and a back azimuth of 49.8°. Analysis of drone video, obtained during this firework show, indicates that the back azimuth of the launch site was approximately 52°, which is in excellent agreement given that the back azimuths of the burst locations varied during the performance (i.e., not every firework was shot directly upward). The firework show on 4 July 2021 was partially recorded since the data acquisition system required a reset during the first part of the show. The show ended at 02:57 UTC with the final 20 min recorded. The precise launch sites were confirmed by inspecting the peninsula used for the launches after the show, which both launch sites were close to each other with a back azimuth of 45°. Time trace and spectrograms clearly capture each individual burst, and FK analysis produced similar results to the 2018 event. Both of these events are excellent checks to confirm data handling, processing, and beamforming when using this database.

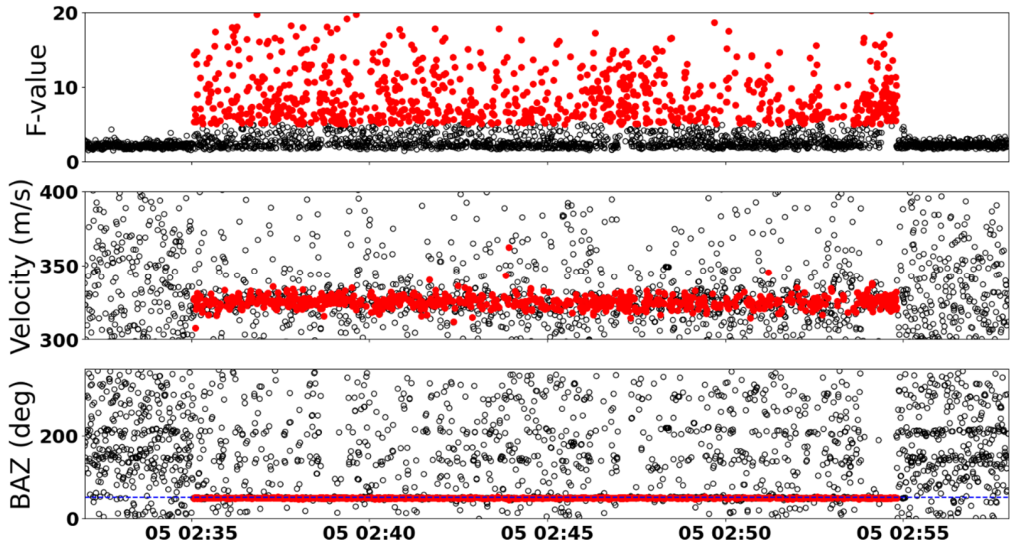

Figure 9. FK analysis results including (**top**) F-value, (**middle**) trace velocity, and (**bottom**) back azimuth during the Stillwater, Oklahoma firework show on 4 July 2018. Closed (red) markers indicate periods with high coherence (i.e., high F-value) and an acoustic trace velocity.

3.2.3. Aircraft

Aircrafts are a very common low-audible event detected by OSU1 since the array was located approximately 3 km directly to the south of the Stillwater Regional Airport (SWO). While SWO is not a major international airport, it does have one major carrier with multiple daily flights and houses the OSU aviation program. Consequently, there are smaller airplanes flown in the area at all times of the day throughout the year as well as periodic larger airplanes. In addition, there are multiple military bases in the region, including Tinker Air Force Base, which results in semi-frequent passes by military aircraft and helicopters. Figure 10 shows the time trace and spectrogram from a period on 11 August 2022 when eyewitnesses were at OSU1 confirming flyovers by multiple smaller general aviation airplanes. The error-function shaped curves in the spectrogram are characteristic acoustic signatures of airplanes passing over the array. The frequency shift is due to the Doppler effect, a well-known phenomenon that the frequency at a receiver (observer) shifts based on the relative motion between the source and receiver. The observed frequency shift can be used to determine the airplane position and speed [58,59]. Specifically, higher frequencies occur when the source (airplane) moves toward the receiver (observer), and lower frequencies occur when the source (airplane) moves away from the receiver (observer). On the day shown in Figure 10, there was one particular airplane that was making turns almost directly over OSU1, which could explain the oscillation in frequency right after it passed over OSU1. Given that the receiver (OSU1) was not moving, the airplane speed (V_s) is readily determined from the shift in frequency as $V_s = c(f_{high} - f_{low})/(f_{high} + f_{low})$, where c is the speed of sound, and f is the received frequency when it was (high) moving toward or (low) away from OSU1. For example, the strongest spike in the time trace in Figure 10 has an initial (high) and final (low) frequency of 104 and 76 Hz, respectively. If the speed of sound was ~343 m/s, the corresponding airplane speed would be 52.8 m/s (118 mph), which is consistent with the lower end of small propeller airplanes as the one flying over OSU1 on this day. Therefore, this dataset provides a large sample of airplane flyovers during a wide range of operation and atmospheric conditions.

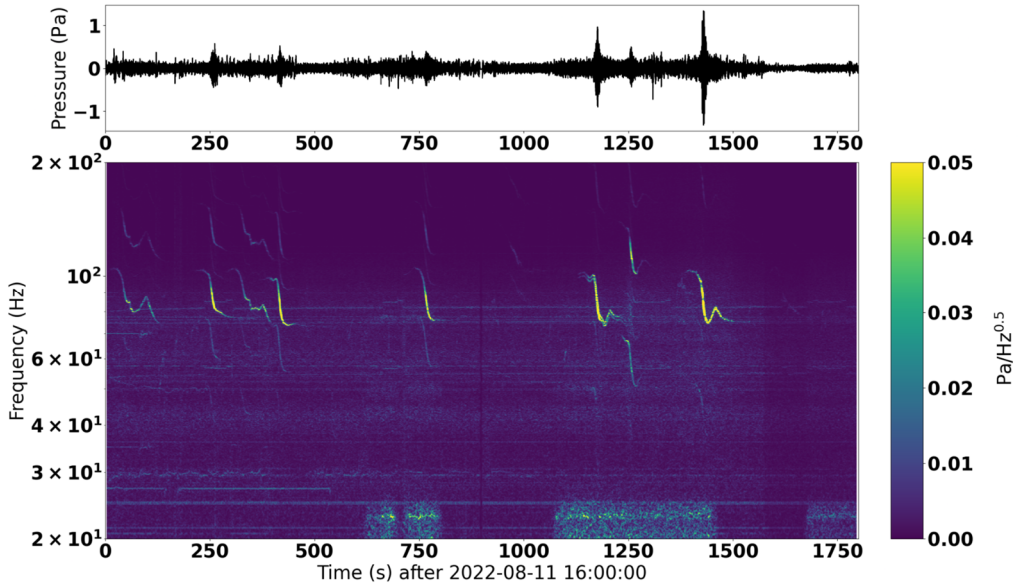

Figure 10. (**top**) Time trace and (**bottom**) spectrogram of OSU1 data during confirmed flyovers by multiple airplanes on 11 August 2022. Time is measured relative to 16:00 UTC on 11 August 2022.

3.2.4. Explosions

Detection of explosions is a major application of infrasound arrays, specifically for use in the CTBT. Beginning in 2019, Oklahoma has been a unique location to study explosions due to the discovery by the Oklahoma Geological Survey (OGS) of an anthropogenic acoustic anomaly all across Oklahoma and neighboring states [60]. This was eventually determined to be infrasonic waves traveling from the McAlester Army Ammunition Plant (MCAAP) in McAlester, Oklahoma that were created from the disposal of munitions via detonations. The munition detonations typically occur daily (except for Sundays) in two sets starting at approximately 16:00 UTC. Each set has between 5000 and 60,000 lbs of munitions destroyed using roughly 25 smaller detonations at 20 s intervals [13]. The detonation sites are ~180 km from OSU1, which given their regularity makes them a good reference source. In fact, they were used in several recent studies to investigate short temporal atmospheric variations in the troposphere [14] and stratosphere [61]. The OSU1 data were initially analyzed using a 0.1 to 20 Hz bandpass filter and 10 s windows on the dates of confirmed detonations listed in Carmichael et al. [13]. From this initial pass, there were ~50 days where clear arrivals matched expected infrasonic signatures from the detonations. One of these dates was 25 June 2019, which had strong arrivals at OSU1-N, as seen in the time trace and spectrogram provided in Figure 11. Inspection of this spectrogram reveals precisely two sets of 26 detonations, which matches ground truth information [13]. These detections were verified using FK analysis to confirm that the back azimuth (~145°) and trace velocities were consistent with acoustic arrivals from the MCAAP site. Detonations have continued beyond those reported in Carmichael et al. [13] with confirmations at OSU1 in July 2022 as well as reports from other infrasound studies [14], including at least one observation from a heliotrope [62] at an altitude of ~20 km [17]. The MCAAP detonations recorded at OSU1 provide a rich dataset that should be further analyzed, especially the propagation conditions that lead to detection or no detections at OSU1. In addition, an investigation into explosive yield (perhaps quantified by local seismic motions when ground truth is not available) versus amplitude could provide significant insights into transmission loss.

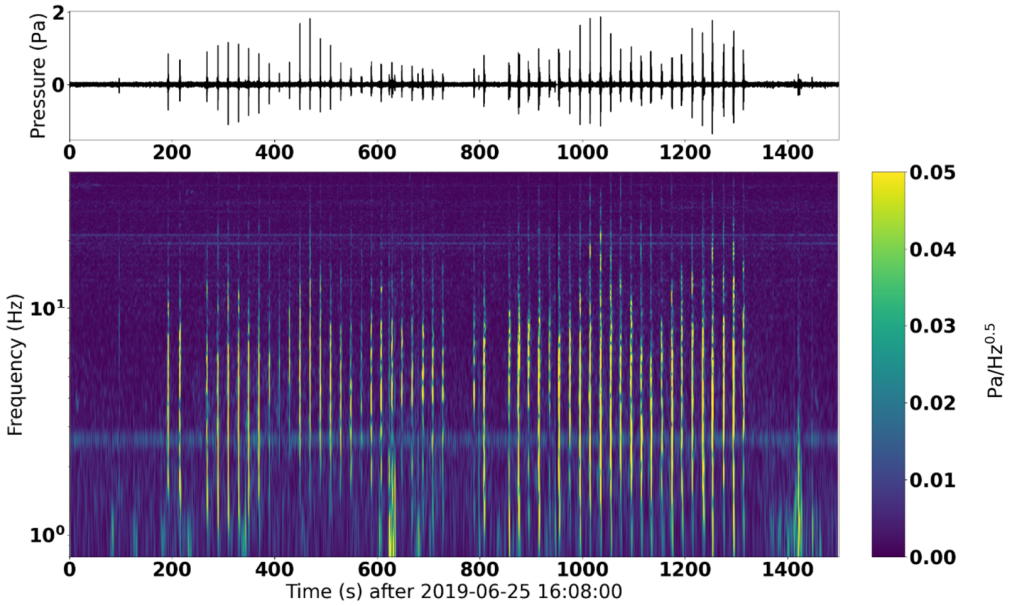

Figure 11. (**top**) Time trace and (**bottom**) spectrogram of OSU1-N on 25 June 2019 during the period when acoustic arrivals from MCAAP munition detonations were confirmed. Time is measured in seconds relative to 16:08 UTC.

3.2.5. Bolides

Fireballs are very bright meteors, and bolides are particularly bright fireballs that often explode. Some are sufficiently large and fast to produce shockwaves and infrasound [63,64], which under specific conditions can be detected all across the earth [65]. The NASA Center for Near Earth Object Studies (CNEOS) keeps a list of reported fireball events (cneos.jpl.nasa.gov/fireballs, accessed on 2 March 2023) dating back to 1988. More recently, it was discovered that the NOAA GOES 16 and 17 satellites could be utilized to detect bolides [66,67]. Subsequently, a separate database (neo-bolide.ndc.nasa.gov, accessed on 2 March 2023) was established that used the method outlined in Rumpf et al. [68] for detecting bolides using the Geostationary Lightning Mapper (GLM) aboard the GOES weather satellites. One of the bolides identified by both GOES satellites using the GLM-based algorithm occurred on 4 April 2019 at 22:19:01 UTC. The bolide's latitude and longitude were 35.3° and −93.9°, respectively, which places it within ~300 km of OSU1. The FK analysis results, with the data bandpass filtered between 0.5 and 10 Hz and analyzed with 10 s windows and 75% overlap, are shown in Figure 12. A strong coherent signal (i.e., high F-value) arrived at OSU1 14 min after the reported occurrence (22:33 UTC) with an average azimuth angle of 95.8°, which is slightly lower than that based on the reported location (107°). Dr. E.A. Silber notes that the reported time/location is associated with the point of maximum energy deposition, or a single point along the meteor trajectory (personal communication, 3 November 2022). This is a potential cause for the discrepancy between angles, though a more detailed analysis of the event would be required to determine the cause. Moreover, the arrival was slightly faster than expected since the fastest time of arrival (i.e., pure horizontal propagation) would have arrived 42 s later.

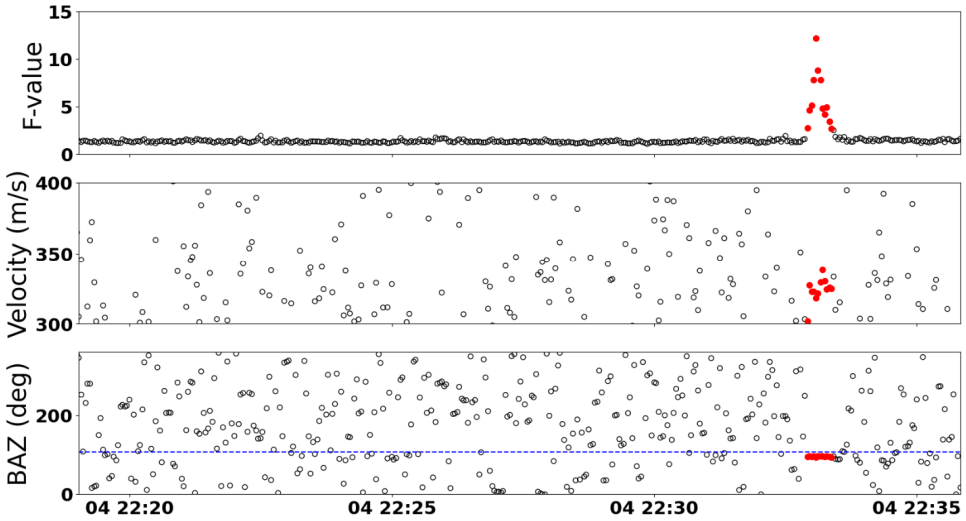

Figure 12. FK analysis results indicating the detection of a strong coherent signal, which was nominally consistent with a reported bolide/fireball identified by the GOES satellites at 22:19:01 UTC on 4 April 2019 and was ~300 km from OSU1. The blue dashed line marks the back azimuth angle of the reported bolide. Closed (red) markers indicate periods with high coherence (i.e., high F-value) and an acoustic trace velocity.

A range independent 2D ray-tracing simulation was performed to assess whether ground-based sensors ~300 km from the bolide were likely to receive the infrasound signal. For the simulation, the source height was set at 40 km and a Ground-to-Space (G2S) model [69] profile was obtained from the NCPA G2S Request System (g2s.ncpa.olemiss.edu, accessed on 2 March 2023). The source height of 40 km was selected as an estimated height based on similar events in the CNEOS database, due to the fact that no altitude was listed for this specific event. The effective sound speed profile and the resulting ray traces are shown in Figure 13. The simulation indicates that a ground detection was not likely before ~240 km, but at OSU1 (marked with a black triangle) there was minimal transmission loss. Given the high probability of detection and the low resolution of the reported position, this was likely a detection of the bolide and its early arrival could provide insight into the flight path relative to OSU1. Another fireball was investigated, which occurred on 2 February 2019 near western Cuba. Analysis of OSU1 data at the expected arrival time revealed no clear signal detection. Pilger et al. [70] analyzed this fireball and indicated detections at IMS network stations on the east coast of the United States, but not those with a similar back azimuth to OSU1 (IS56, IS57, and IS53). These were the only two bolide/fireball events investigated.

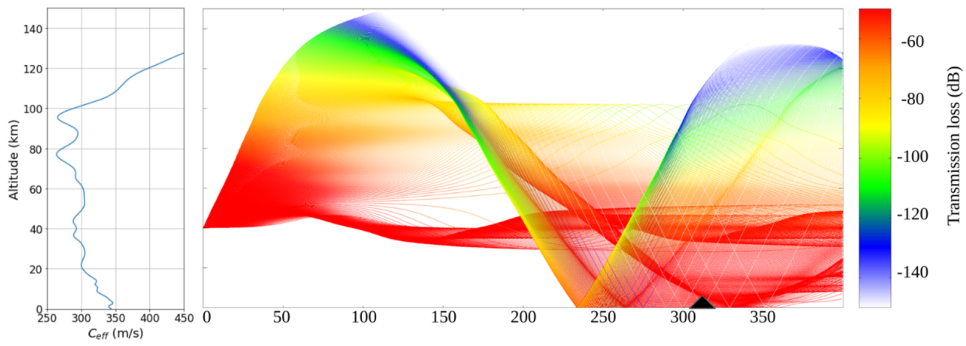

Figure 13. (**left**) Ground-to-space (G2S) effective sound speed profile and (**right**) 2D ray-tracing simulation results, indicating that ground-based sensing at OSU1 (marked with the black triangle) was likely.

3.2.6. Earthquakes

One of the most commonly studied sources of infrasound are earthquakes. During the start of the OSU1 deployment, Oklahoma became the state within the contiguous US with the most earthquakes. Infrasound generated from earthquakes are commonly divided into epicentral [71], local [72], and secondary [73]. Epicentral infrasound refers to the acoustic waves produced by the strong ground motion at the epicenter of an earthquake. Local infrasound is seismo-acoustic coupling at a location near the receiver. Finally, secondary infrasound is the seismic wave interacting with topological features, which emits infrasound waves as a source of their own. Large earthquakes have been detected over very large distances (>1000 km) [74], while smaller earthquakes have been detected on a regional scale [75]. A non-acoustic detection can be made on infrasound sensors through the direct coupling of the seismic wave with the infrasound sensor and the structure holding the sensor. These seismically coupled signals can be difficult to distinguish from local infrasound. For example, the largest earthquake in the history of the state of Oklahoma was a 5.8 M_w earthquake on 3 September 2016 at 12:02:44 UTC, which occurred less than 24 h after the first OSU1 sensor began recording. The shallow strike-slip earthquake occurred 35.1 km to the northeast of OSU1 at a depth of 5.6 km. The time trace and spectrogram from OSU1-W following this earthquake are shown in Figure 14 with lines marking the event time, seismic estimated time of arrival (ETA), acoustic ETA, and an observed audible arrival. The seismic arrivals include the ETA for the high broadband sampled north-south (HHN) and vertical (HHZ) velocity. This shows that the strong signal was due to the seismic arrivals with the 1–10 Hz content aligned with the HHZ ETA and the higher frequency content more aligned with the HHN ETA. The audible arrival appears shortly after the direct path acoustic ETA with significant spectral content between 30 and 70 Hz. This gives the audible arrival a celerity of 250 m/s. Note that the data were bandpass filtered from 20–200 Hz, which if lower frequency content were included, the audible arrival is not apparent. There are significantly more earthquakes that are not examined, which occurred during the OSU1 deployment, especially during the first year (e.g., nearly 300 earthquakes with 3 M_w or greater occurred in 2017).

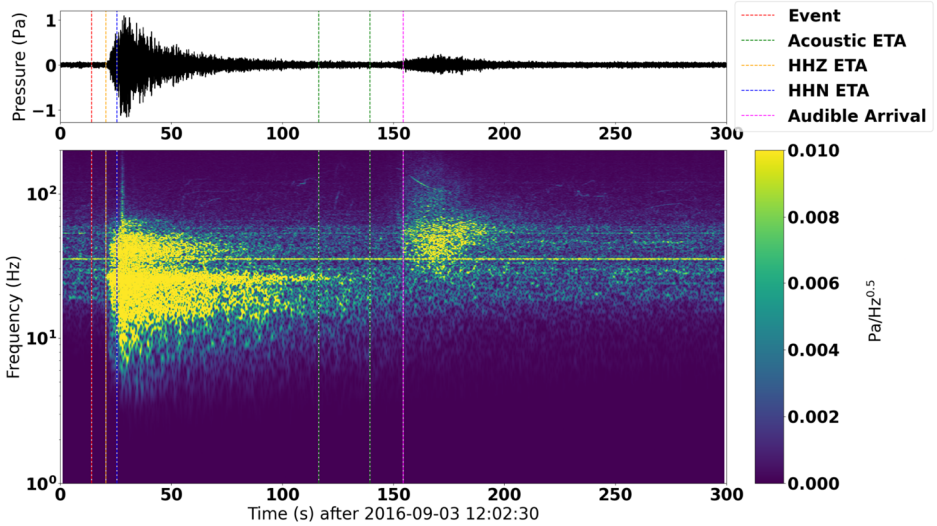

Figure 14. (**top**) Time trace and (**bottom**) spectrogram of OSU1-W during the 5.8 M_w earthquake that occurred on 3 September 2016.

3.2.7. Severe Weather

OSU1 was deployed primarily for studying infrasound produced from severe weather with an emphasis on tornadoes. Severe weather infrasound has been linked to lightning [76], sprites [77], hurricanes [78], funnel clouds [79], and tornadoes [10,80,81]. Elbing et al. [11] reported OSU1 data from a small tornado of unknown intensity on the Enhanced Fujita

(EF) scale (i.e., EFU) that occurred on 11 May 2017 and was 18.7 km from OSU1. The data were contaminated with wind noise below ~5 Hz, but a spectral peak at ~8.3 Hz was associated with the tornadic activities. The peak was 18 dB above pre-tornado levels and appeared to have non-harmonic overtones. Petrin and Elbing [79] also report on OSU1 data from an EF1 tornado on 6 May 2019, which showed no significant rise in infrasound, even though it was only 19.4 km from OSU1. The infrasound propagation from this tornado was simulated using a Wide-Angled Pade Parabolic Equation (PAPE) within NCPAprop [82], along with composite Ground-to-Space (G2S) atmospheric profiles from AVO-G2S [83], in order to estimate the transmission loss at the ground in the direction of OSU1. These results showed that infrasound propagation from this tornado to OSU1 was unfavorable and ground-based sensing was unlikely. However, it should be noted that about 20 min later, the storm system that produced this tornado passed directly over OSU1 and a spectral peak formed at about 8 Hz with overtones similar to those reported by Elbing et al. [11].

Two weeks later on 18 May 2019, an EF0 tornado formed at 14:27 UTC near Stillwater, Oklahoma (36.106°, −97.002°), which was 7.8 km east-southeast of OSU1. This was a Quasi-Linear Convective System (QLCS) tornado that had a damage width of 22.9 m and length of 0.32 km. The PAPE infrasound propagation simulation, with AVO-G2S atmospheric profiles for an 8 Hz signal emitted from this tornado location, showed minimal transmission loss at the OSU1 location, which indicates a high probability of detection for this tornado with OSU1. The OSU1 power spectra before, during, and after the tornado are shown in Figure 15. Each period was 30 min long, with the "before" starting 1 h before the tornado touchdown, the "during" beginning at touchdown and extending until the storm passed over OSU1, and the "after" period beginning 30 min after the storm passed over OSU1. The signal was bandpass filtered between 0.5 and 50 Hz, and each spectrum was produced using the Welch method with 50 s segments and 75% overlap. The slope from 1 to 4 Hz is indicative of wind noise, in which this trend extends down to at least 0.1 Hz if the data had not been bandpass filtered. Rising out of that gradual slope is a broadband peak nominally at 8 Hz, with some non-harmonic overtones. This behavior is nearly identical to the EFU tornado reported by Elbing et al. [11], which both of these tornadoes were of similar size. Of note, the spectral structure persists in the after period, but at a significantly reduced amplitude. This requires further investigation; however, the 2017 tornado [11] exhibited a similar behavior with the persistence of the acoustic structure.

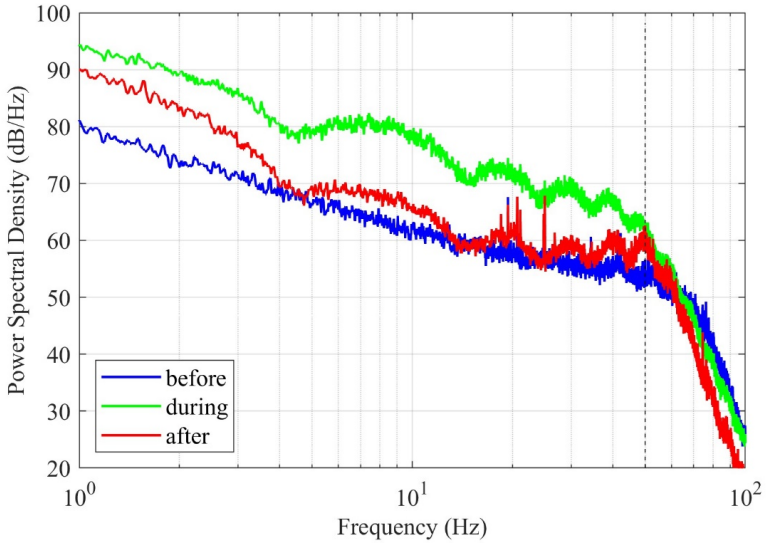

Figure 15. The averaged power spectral density from OSU1-W from 18 May 2019 for the period before (30–60 min before the EF0 tornado), during (from touchdown at 14:27 UTC until the storm passed OSU1), and after (30–60 min after the storm passed OSU1) the QLCS tornado. Vertical dashed line marks the cutoff frequency.

4. Discussion

The results of this paper serve the research community in three ways: (i) They provide a unique database within a region of high interest for infrasound, (ii) they provide a broad overview of acoustic detections and the means to identify them, and (iii) they introduce the research community to the availability of these data. First, the OSU1 deployment is unique due to the combination of being a long-term deployment (over 6 years) recording the infrasound and low-audible range at a relatively high sample rate (1000 Hz). Most long-term infrasound deployments have sample rates at or below 40 Hz (e.g., IRIS BDF channel samples at 40 Hz), which impacts the resolution for beamforming as well as the range of detectable sources. Then, as mentioned previously and highlighted by some of the selected examples, OSU1 is located in a region where many interesting infrasound signatures are present and studied by multiple teams (e.g., MCAAP munition detonations, frequent tornadoes, Venus seismology analog study, etc.). Second, the overview of different sources in the same region is of importance for any infrasound study since one challenge of infrasound research is the ability to discriminate between a source of interest and other local/global sources. For example, the International Monitoring System (IMS) of the Comprehensive Nuclear Test Ban Treaty Organization (CTBTO) performs global monitoring for nuclear tests [28], and it is critical that they are able to differentiate between a bolide burst (e.g., [84–86]) and an anthropogenic source. For this reason, most atmospheric infrasound researchers regularly work to establish the infrasound signatures of other known sources, in which these results provide a broad overview of common sources. Finally, each of the sources discussed have the potential for a more in-depth analysis and a broader search within the OSU1 database. The OSU1 data presented are publicly available [31], and all data are available upon reasonable request.

The observed variation in the microbarom peak frequency with amplitude (or season) is an example of an area that could be further explored. The frequency variation could imply that the microbarom source was different between seasons, which is supported by recent microbarom theory and modelling [87,88]. The mechanism responsible for these varying source locations is related to the change in stratospheric winds through the year, which brings microbarom signals from different regions. Therefore, the observed microbarom variation presented in this study can be compared against suggested source locations and historic stratospheric wind profiles to gain further insight into the cause. This method of analyzing the atmospheric structure utilizing infrasonic detections can also be utilized for regional sources, such as the MCAAP detonations and bolides, where the ability to discern directionally is preserved (due to the higher frequency of the arriving signals). This technique has shown promise for studying propagation patterns in Averbuch et al. [14,61], where the MCAAP detonations were used to observe short-term stratospheric and tropospheric variations.

Another example of an area that could be further explored is the analysis of the power spectral density from tornadoes (e.g., Figure 15) to identify the fluid mechanism responsible for its production. The classical analysis [89] assumed that it was produced from radial oscillations of the tornado vortex core. This analysis modelled the tornado as a compressible Rankine vortex constrained to axisymmetric vibrations. It predicts spectral peaks in the infrasound at frequencies inversely related to the tornado size, $f_n = (4n + 5)c/4d_c$. Here, f_n is the spectral peak in Hz, n is a non-negative integer (mode number), c is the speed of sound, and d_c is the vortex core diameter. For the tornado power spectral density in Figure 15, the fundamental frequency ($n = 0$) peaks between 6.4 and 8.5 Hz. Abdullah [89] predicts a vortex core diameter between 50 and 67 m, which is two to three times larger than the damage width. The overtones in Figure 15 are nominally at 18.2, 28.8, 38.4, and 46.5 Hz, which are well approximated by a linear fit $f_n = 9.83n + 8.18$. The linearly related, non-harmonic overtones are consistent with those predicted by Abdullah [89], but similar to Elbing et al. [11], the slope of the line is larger than predicted. While Abdullah [89] predicts the basic trends of tornado infrasound observations, there are several fundamental issues with the analysis that prevent it from being the fluid mechanism [90]. Recent observations

and analyses suggest that the fluid mechanism(s) responsible for tornado infrasound are related to latent heat effects [91,92], pressure relaxation [93,94], and/or shear instabilities. More research (including observations) is required to identify the specific roles that each of these mechanisms play in the tornado infrasound production, as well as to resolve the reason that the basic radial oscillation analysis produces the general trends.

5. Conclusions

The OSU1 array was operational in the majority of the time between September 2016 and 2022 with a sample rate of 1000 Hz and microphones that had a flat response from 0.1 to 200 Hz. This array deployment provides the research community with a new dataset in a heavily studied environment (Oklahoma, USA). The ambient noise of OSU1 was characterized with a low, median, and high noise model that had similar behavior to global noise models [34,35]. The wind speed dependence of the ambient noise was assessed using the nearby Oklahoma Mesonet site as a consistent local wind measurement. This showed a steady rise in broadband noise with increasing speed with a nominal increase of 1 to 1.5 dB/Hz increase per m/s increase. Detections of microbaroms, fireworks, airplanes, munition explosions, bolides, earthquakes (acoustic and seismic), and tornadoes are reported. Each detection used a combination of time trace, power spectral density, spectrogram, and beamforming analysis based on the type of source. The detections reported are only a subset of many more events that can be found and analyzed with further investigations.

Author Contributions: Conceptualization, T.C.W. and B.R.E.; methodology, T.C.W., C.E.P. and B.R.E.; software, T.C.W.; validation, T.C.W., C.E.P. and B.R.E.; formal analysis, T.C.W. and B.R.E.; investigation, T.C.W.; resources, B.R.E.; data curation, T.C.W.; writing—original draft preparation, T.C.W.; writing—review and editing, T.C.W. and B.R.E.; visualization, T.C.W. and C.E.P.; supervision, B.R.E.; project administration, B.R.E.; funding acquisition, B.R.E. All authors have read and agreed to the published version of the manuscript.

Funding: This research was funded by the National Science Foundation (NSF) under grant 1539070 (Dr. Tim VanReken, program manager) and by NOAA under grants NA18OAR4590307 and NA19OAR4590340 (Dr. Mark Vincent, program manager). The content of this paper does not necessarily reflect the position or the policy of the US Government, and no official endorsement should be inferred.

Data Availability Statement: All data presented in this study are publicly available via Wilson and Elbing [31]. Additional data are available upon request from the corresponding author.

Acknowledgments: The authors would like to thank the team who originally deployed OSU1 (Arnesha Threatt, Collin Boettcher, Joe Conner, Shannon Maher, Alexis Vance, Jalen Golphin, Jared Hartzler, Jacquelyne Baade) and the team of students who have maintained the array over the years (Real KC, Shelby Webb, Bryce Lindsey).

Conflicts of Interest: The authors declare no conflict of interest.

References

1. Brock, F.V.; Crawford, K.C.; Elliott, R.L.; Cuperus, G.W.; Stadler, S.J.; Johnson, H.L.; Eilts, M.D. The Oklahoma Mesonet: A technical overview. *J. Atmos. Ocean Technol.* **1995**, *12*, 5–19. [CrossRef]
2. Zhang, H.; Jin, M.S.; Leach, M. A study of the Oklahoma City urban heat island effect using a WRF/single-layer urban canopy model, a joint urban 2003 field campaign, and MODIS satellite observations. *Climate* **2017**, *5*, 72. [CrossRef]
3. Wulfmeyer, V.; Turner, D.D.; Baker, B.; Banta, R.; Behrendt, A.; Bonin, T.; Brewer, W.A.; Buban, M.; Choukulkar, A.; Dumas, E.; et al. A new research approach for observing and characterizing land-atmosphere feedback. *Bull. Am. Meteorol. Soc.* **2018**, *99*, 1639–1667. [CrossRef]
4. Asher, E.; Thornberry, T.; Fahey, D.W.; McComiskey, A.; Carslaw, K.; Grunau, S.; Chang, K.-L.; Telg, H.; Chen, P.; Gao, R.-S. A novel network-based approach to determining measurement representation error for model evaluation of aerosol microphysical properties. *J. Geophys. Res. Atmos.* **2022**, *127*, e2021JD035485. [CrossRef]
5. Elbing, B.R.; Gaeta, R.J. Integration of infrasonic sensing with UAS. In Proceedings of the AIAA Aviation Forum 2016, AIAA2016-3581, Washington, DC, USA, 13–17 June 2016. [CrossRef]

6. Hemingway, B.L.; Frazier, A.E.; Ebing, B.R.; Jacob, J.D. Vertical sampling scales for atmospheric boundary layer measurements from small unmanned aircraft systems (sUAS). *Atmosphere* **2017**, *8*, 176. [CrossRef]
7. Smith, S.W.; Chilson, P.B.; Houston, A.L.; Jacob, J.D. Catalyzing collaboration for multi-disciplinary UAS development with a flight campaign focused on meteorology and atmospheric physics. In Proceedings of the AIAA Information Systems 2017, AIAA2017-1156, Grapevine, TX, USA, 9–13 January 2017. [CrossRef]
8. Jacob, J.D.; Chilson, P.B.; Houston, A.L.; Smith, S.W. Considerations for atmospheric measurements with small unmanned aircraft systems. *Atmosphere* **2018**, *9*, 252. [CrossRef]
9. Wilson, T.C.; Brenner, J.; Morrison, Z.; Jacob, J.D.; Elbing, B.R. Wind speed statistics from a small UAS and its sensitivity to sensor location. *Atmosphere* **2022**, *13*, 443. [CrossRef]
10. Frazier, W.G.; Talmadge, C.; Park, J.; Waxler, R.; Assink, J. Acoustic detection, tracking, and characterization of three tornadoes. *J. Acoust. Soc. Am.* **2014**, *135*, 1742–1751. [CrossRef] [PubMed]
11. Elbing, B.R.; Petrin, C.E.; van Den Broeke, M.S. Measurement and characterization of infrasound from a tornado producing storm. *J. Acoust. Soc. Am.* **2019**, *146*, 1528–1540. [CrossRef] [PubMed]
12. White, B.C.; Elbing, B.R.; Faruque, I. Infrasound measurement system for real-time in-situ tornado measurements. *Atmos. Meas. Tech.* **2022**, *15*, 2923–2938. [CrossRef]
13. Carmichael, J.D.; Thiel, A.D.; Blom, P.S.; Walter, J.I.; Dannemann Dugick, F.; Arrowsmith, S.J.; Carr, C.G. Persistent, 'mysterious' seismoacoustic signals reported in Oklahoma state during 2019. *Bull. Seismol. Soc. Am.* **2021**, *112*, 553–574. [CrossRef]
14. Averbuch, G.; Ronac-Giannone, M.; Arrowsmith, S.; Anderson, J.F. Evidence for short temporal atmospheric variations observed by infrasonic signals: 1. The Troposphere. *Earth Space Sci.* **2022**, *9*, e2021EA002036. [CrossRef]
15. Martire, L.; Krishnamoorthy, S.; Komjathy, A.; Bowman, D.; Jacob, J.; Elbing, B.; Hough, E.; Yap, Z.; Lammes, M.; Linzy, H.; et al. A midsummer flights' dream: Balloon-borne infrasound-based aerial seismology. *J. Acoust. Soc. Am.* **2021**, *150*, A180. [CrossRef]
16. Bowman, D.C. Airborne infrasound makes a splash. *Geophys. Res. Lett.* **2021**, *48*, e2021GL096326. [CrossRef]
17. Hough, E.; Ngo, A.; Swaim, T.; Yap, Z.; Vance, A.; Elbing, B.; Jacob, J. Solar balloon development for high altitude observations. In Proceedings of the 2022 Aviation Forum, AIAA2022-4113, Chicago, IL, USA, 27 June–1 July 2022. [CrossRef]
18. Garrett, M.A. Radio astronomy transformed: Aperture arrays—Past, present and future. In Proceedings of the 2013 Africon, Pointe-Aux-Piments, Mauritius, 9–12 September 2013; pp. 1–5. [CrossRef]
19. Den Ouden, O.F.C.; Assink, J.D.; Smets, P.S.M.; Shani-Kadmiel, S.; Averbuch, G.; Evers, L.G. CLEAN beamforming for the enhanced detection of multiple infrasonic sources. *Geophys. J. Int.* **2020**, *221*, 305–317. [CrossRef]
20. Drob, D.P.; Meier, R.R.; Picone, J.M.; Garcés, M.M. Inversion of infrasound signals for passive atmospheric remote sensing. In *Infrasound Monitoring for Atmospheric Studies*; Le Pichon, A., Blanc, E., Hauchecorne, A., Eds.; Springer: Dordrecht, The Netherlands, 2010; pp. 701–731.
21. Mutschlecner, J.P.; Whitaker, R.W. Infrasound from earthquakes. *J. Geophys. Res. Atmos.* **2005**, *110*, D01108. [CrossRef]
22. Lacroix, A.; Farges, T.; Marchiano, R.; Coulouvrat, F. Acoustical measurement of natural lightning flashes: Reconstructions and statistical analysis of energy spectra. *J. Geophys. Res. Atmos.* **2018**, *123*, 12040–12065. [CrossRef]
23. Pilger, C.; Ceranna, L.; Le Pichon, A.; Brown, P. Large meteoroids as global infrasound reference events. In *Infrasound Monitoring for Atmospheric Studies*, 2nd ed.; Le Pichon, A., Blanc, E., Hauchecorne, A., Eds.; Springer: Dordrecht, The Netherlands, 2019; pp. 451–470.
24. Assink, J.D.; Averbuch, G.; Smets, P.S.M.; Evers, L.G. On the infrasound detected from the 2013 and 2016 DPRK's underground nuclear tests. *Geophys. Res. Lett.* **2016**, *43*, 3526–3533. [CrossRef]
25. Campus, P.; Christie, D.R. Worldwide observations of infrasonic waves. In *Infrasound Monitoring for Atmospheric Studies*; Le Pichon, A., Blanc, E., Hauchecorne, A., Eds.; Springer: Dordrecht, The Netherlands, 2010; pp. 185–234.
26. Mayer, S.; van Herwijnen, A.; Ulivieri, G.; Schweizer, J. Evaluating the performance of an operational infrasound avalanche detection system at three locations in the Swiss Alps during two winter seasons. *Cold Reg. Sci. Technol.* **2020**, *173*, 102962. [CrossRef]
27. Johnson, J.B. Generation and propagation of infrasonic airwaves from volcanic explosions. *J. Volcanol. Geoth. Res.* **2003**, *121*, 1–14. [CrossRef]
28. Marty, J. The IMS infrasound network: Current status and technological developments. In *Infrasound Monitoring for Atmospheric Studies*, 2nd ed.; Le Pichon, A., Blanc, E., Hauchecorne, A., Eds.; Springer: Dordrecht, The Netherlands, 2019; pp. 3–62.
29. Assink, J.; Averbuch, G.; Shani-Kadmiel, S.; Smets, P.; Evers, L. A seismo-acoustic analysis of the 2017 North Korean nuclear test. *Seismol. Res. Lett.* **2018**, *89*, 2025–2033. [CrossRef]
30. Koch, K.; Pilger, C. Infrasound observations from the site of past underground nuclear explosions in North Korea. *Geophys. J. Int.* **2019**, *216*, 182–200. [CrossRef]
31. Wilson, T.; Elbing, B. Infrasonic sources detected on OSU1. *Figshare* **2023**, 2. [CrossRef]
32. Hart, D.; McDonald, T. Infrasound sensor and porous-hose filter evaluation results. In Proceedings of the 2009 Monitoring Research Review: Ground-Based Nuclear Explosion Monitoring Technologies, Denver, CO, USA, 25–27 September 2009; Volume 9, pp. 735–741.
33. Threatt, A.R. Investigation of Natural and Anthropomorphic Sources of Atmospheric Infrasound. Master's Thesis, Oklahoma State University, Stillwater, OK, USA, 2016.

34. Brown, D.; Ceranna, L.; Prior, M.; Mialle, P.; Le Bras, R.J. The IDC seismic, hydroacoustic and infrasound global low and high noise models. *Pure Appl. Geophys.* **2014**, *171*, 361–375. [CrossRef]
35. Marty, J.; Doury, B.; Kramer, A. Low and high broadband spectral models of atmospheric pressure fluctuation. *J. Atmos. Ocean Technol.* **2021**, *38*, 1813–1822. [CrossRef]
36. Capon, J. High-resolution frequency-wavenumber spectrum analysis. *Proc. IEEE* **1969**, *57*, 1408–1418. [CrossRef]
37. Denholm-Price, J.C.W.; Rees, J.M. Detecting waves using an array of sensors. *Mon. Weather Rev.* **1999**, *127*, 57–69. [CrossRef]
38. Evers, L.G. The Inaudible Symphony: On the Detection and Source Identification of Atmospheric Infrasound. Ph.D. Thesis, Delft University of Technology, Delft, The Netherlands, 2008.
39. McPherson, R.A.; Fiebrich, C.; Crawford, K.C.; Elliott, R.L.; Kilby, J.R.; Grimsley, D.L.; Martinez, J.E.; Basara, J.B.; Illston, B.G.; Morris, D.A.; et al. Statewide monitoring of the mesoscale environment: A technical update on the Oklahoma Mesonet. *J. Atmos. Ocean Technol.* **2007**, *24*, 301–321. [CrossRef]
40. Welch, P. The use of fast Fourier transform for the estimation of power spectra: A method based on time averaging over short, modified periodograms. *IEEE Trans. Audio Electroacoust.* **1967**, *15*, 70–73. [CrossRef]
41. Beyreuther, M.; Barsch, R.; Krischer, L.; Megies, T.; Behr, Y.; Wassermann, J. ObsPy: A Python toolbox for seismology. *Seismol. Res. Lett.* **2010**, *81*, 530–533. [CrossRef]
42. Krischer, L.; Megies, T.; Barsch, R.; Beyreuther, M.; Lecocq, T.; Caudron, C.; Wassermann, J. ObsPy: A bridge for seismology into the scientific Python ecosystem. *Comput. Sci. Discov.* **2015**, *8*, 014003. [CrossRef]
43. Blom, P.S.; Marcillo, O.E.; Euler, G.G. *InfraPy: Python-Based Signal Analysis Tools for Infrasound; LANL Technical Report 2016*; No. LA-UR-16-24234; Los Alamos National Lab: Los Alamos, NM, USA, 2016.
44. McComas, S.; Arrowsmith, S.; Hayward, C.; Stump, B.; McKenna Taylor, M.H. Quantifying low-frequency acoustic fields in urban environments. *Geophys. J. Int.* **2022**, *229*, 1152–1174. [CrossRef]
45. Cansi, Y. An automatic seismic event processing for detection and location: The P.M.C.C. Method. *Geophys. Res. Lett.* **1995**, *22*, 1021–1024. [CrossRef]
46. Rost, S.; Thomas, C. Array seismology: Methods and applications. *Rev. Geophys.* **2002**, *40*, 2.1–2.27. [CrossRef]
47. Bowman, J.R.; Baker, G.E.; Bahavar, M. Ambient infrasound noise. *Geophys. Res. Lett.* **2005**, *32*, L09803. [CrossRef]
48. Pepyne, D.L.; Klaiber, S. Highlights from the 2011 CASA infrasound field experiment. In Proceedings of the 92nd American Meteorological Society Annual Meeting, New Orleans, LA, USA, 22–26 January 2012.
49. Benioff, H.; Gutenberg, B. Waves and currents recorded by electromagnetic barographs. *Bull. Am. Meteorol. Soc.* **1939**, *20*, 421–428. [CrossRef]
50. Donn, W.L.; Naini, B. Sea wave origin of microbaroms and microseisms. *J. Geophys. Res.* **1973**, *78*, 4482–4488. [CrossRef]
51. Sutherland, L.C.; Bass, H.E. Atmospheric absorption in the atmosphere up to 160 km. *J. Acoust. Soc. Am.* **2004**, *115*, 1012–1032. [CrossRef]
52. Waxler, R.; Gilbert, K.E. The radiation of atmospheric microbaroms by ocean waves. *J. Acoust. Soc. Am.* **2006**, *119*, 2651–2664. [CrossRef]
53. Bowman, D.C.; Lees, J.M. Infrasound in the middle stratosphere measured with a free-flying acoustic array. *Geophys. Res. Lett.* **2015**, *42*, 10,010–10,017. [CrossRef]
54. Landés, M.; Le Pichon, A.; Shapiro, N.M.; Hillers, G.; Campillo, M. Explaining global patterns of microbarom observations with wave action models. *Geophys. J. Int.* **2014**, *199*, 1328–1337. [CrossRef]
55. Smirnov, A.; De Carlo, M.; Le Pichon, A.; Shapiro, N.M.; Kulichkov, S. Characterizing the oceanic ambient noise as recorded by the dense seismo-acoustic Kazakh network. *Solid Earth* **2021**, *12*, 503–520. [CrossRef]
56. Le Pichon, A.; Ceranna, L.; Garcés, M.; Drob, D.; Millet, C. On using infrasound from interacting ocean swells for global continuous measurements of winds and temperature in the stratosphere. *J. Geophys. Res.* **2006**, *111*, D11106. [CrossRef]
57. Batubara, M.; Yamamoto, M.Y. Infrasonic observation of microbarom signals in the middle latitude: An investigation of summer and winter season on the upper atmosphere. *J. Phys. Conf. Ser.* **2021**, *1896*, 012001. [CrossRef]
58. Torney, D.C. Localization and observability of aircraft via Doppler shifts. *IEEE Trans. Aerosp. Electron. Syst.* **2007**, *43*, 1163–1168. [CrossRef]
59. Martin, S.R.; Genesca, M.; Romeu, J.; Arcos, R. Passive acoustic method for aircraft states estimation based on the Doppler effect. *IEEE Trans. Aerosp. Electron. Syst.* **2014**, *50*, 1330–1346. [CrossRef]
60. Thiel, A.D. An Acoustic Anomaly. OK Geological Survey Field Blog. 2019. Available online: https://okgeosurvey.wordpress.com/2019/07/25/an-acoustic-anomaly (accessed on 2 March 2023).
61. Averbuch, G.; Sabatini, R.; Arrowsmith, S. Evidence for short temporal atmospheric variations observed by infrasonic signals: 2. The stratosphere. *Earth Space Sci.* **2022**, *9*, e2022EA002454. [CrossRef]
62. Bowman, D.C.; Norman, P.E.; Pauken, M.T.; Albert, S.A.; Dexheimer, D.; Yang, X.; Krishnamoorthy, S.; Komjathy, A.; Cutts, J.A. Multihour stratospheric flights with the heliotrope solar hot-air balloon. *J. Atmos. Ocean Technol.* **2020**, *37*, 1051–1066. [CrossRef]
63. Silber, E.A.; Boslough, M.; Hocking, W.K.; Gritsevich, M.; Whitaker, R.W. Physics of meteor generated shock waves in the Earth's atmosphere—A review. *Adv. Space Res.* **2018**, *62*, 489–532. [CrossRef]
64. Ens, T.A.; Brown, P.G.; Edwards, W.N.; Silber, E.A. Infrasound production by bolides: A global statistical study. *J. Atmos. Sol. Terr. Phys.* **2012**, *80*, 208–229. [CrossRef]

65. Le Pichon, A.; Ceranna, L.; Pilger, C.; Mialle, P.; Brown, D.; Henry, P.; Brachet, N. The 2013 Russian fireball largest ever detected by CTBTO infrasound sensors. *Geophys. Res. Lett.* **2013**, *40*, 3732–3737. [CrossRef]
66. Goodman, S.J.; Blakeslee, R.J.; Koshak, W.J.; Mach, D.; Bailey, J.; Buechler, D.; Carey, L.; Schultz, C.; Bateman, M.; McCaul, E., Jr.; et al. The GOES-R Geostationary Lightning Mapper (GLM). *Atmos. Res.* **2013**, *125–126*, 34–49. [CrossRef]
67. Jenniskens, P.; Albers, J.; Tillier, C.E.; Edgington, S.F.; Longenbaugh, R.S.; Goodman, S.J.; Rudlosky, S.D.; Hildebrand, A.R.; Hanton, L.; Ciceri, F.; et al. Detection of meteoroid impacts by the Geostationary Lightning Mapper on the GOES-16 satellite. *Meteorit Planet Sci.* **2018**, *53*, 2445–2469. [CrossRef]
68. Rumpf, C.M.; Longenbaugh, R.S.; Henze, C.E.; Chavez, J.C.; Mathias, D.L. An algorithmic approach for detecting bolides with the Geostationary Lightning Mapper. *Sensors* **2019**, *19*, 1008. [CrossRef]
69. Drob, D.P.; Picone, J.M.; Garcés, M. Global morphology of infrasound propagation. *J. Geophys. Res. Atmos.* **2003**, *108*, 4680. [CrossRef]
70. Pilger, C.; Gaebler, P.; Hupe, P.; Ott, T.; Drolshagen, E. Global monitoring and characterization of infrasound signatures by large fireballs. *Atmosphere* **2020**, *11*, 83. [CrossRef]
71. Hill, D.P.; Fischer, F.G.; Lahr, K.M.; Coakley, J.M. Earthquake sounds generated by body-wave ground motion. *Bull. Seismol. Soc. Am.* **1976**, *66*, 1159–1172.
72. Lamb, O.D.; Lees, J.M.; Malin, P.E.; Saarno, T. Audible acoustics from low-magnitude fluid-induced earthquakes in Finland. *Sci. Rep.* **2021**, *11*, 19206. [CrossRef]
73. Arrowsmith, S.J.; Johnson, J.B.; Drob, D.P.; Hedlin, M.A.H. The seismoacoustic wavefield: A new paradigm in studying geophysical phenomena. *Rev. Geophys.* **2010**, *48*, RG4003–RG4023. [CrossRef]
74. Le Pichon, A.; Mialle, P.; Guilbert, J.; Vergoz, J. Multistation infrasonic observations of the Chilean earthquake of 2005 June 13. *Geophys. J. Int.* **2006**, *167*, 838–844. [CrossRef]
75. Johnson, J.B.; Mikesell, T.D.; Anderson, J.F.; Liberty, L.M. Mapping the sources of proximal earthquake infrasound. *Geophys. Res. Lett.* **2020**, *47*, e2020GL091421. [CrossRef]
76. Farges, T.; Hupe, P.; Le Pichon, A.; Ceranna, L.; Listowski, C.; Diawara, A. Infrasound thunder detections across 15 years over Ivory Coast: Localization, propagation, and link with the stratospheric semi-annual oscillation. *Atmosphere* **2021**, *12*, 1188. [CrossRef]
77. Sindelarova, T.; Chum, J.; Skripnikova, K.; Base, J. Atmospheric infrasound observed during intense convective storms on 9–10 July 2011. *J. Atmos. Sol. Terr. Phys.* **2015**, *122*, 66–74. [CrossRef]
78. Hetzer, C.H.; Waxler, R.; Gilbert, K.E.; Talmadge, C.L.; Bass, H.E. Infrasound from hurricanes: Dependence on the ambient ocean surface wave field. *Geophys. Res. Lett.* **2008**, *35*, L14609. [CrossRef]
79. Petrin, C.E.; Elbing, B.R. Infrasound emissions from tornadoes and severe storms compared to potential tornadic generation mechanisms. *Proc. Meet. Acoust.* **2019**, *36*, 045005. [CrossRef]
80. Bedard, A.J. Low-frequency atmospheric acoustic energy associated with vortices produced by thunderstorms. *Mon. Weather Rev.* **2005**, *133*, 241–263. [CrossRef]
81. Dunn, R.W.; Meredith, J.A.; Lamb, A.B.; Kessler, E.G. Detection of atmospheric infrasound with a ring laser interferometer. *J. Appl. Phys.* **2016**, *120*, 123109. [CrossRef]
82. Waxler, R.M.; Assink, J.D. NCPAprop—A software package for infrasound propagation modeling. *J. Acoust. Soc. Am.* **2017**, *141*, 3627. [CrossRef]
83. Schwaiger, H.F.; Iezzi, A.M.; Fee, D. AVO-G2S: A modified, open-source Ground-to-Space atmospheric specification for infrasound modeling. *Comput. Geosci.* **2019**, *125*, 90–97. [CrossRef]
84. Silber, E.A.; Le Pichon, A.; Brown, P.G. Infrasonic detection of a near-Earth object impact over Indonesia on 8 October 2009. *Geophys. Res. Lett.* **2011**, *38*, L12201. [CrossRef]
85. Brown, P.G.; Assink, J.D.; Astiz, L.; Blaauw, R.; Boslough, M.B.; Borovička, J.; Brachet, N.; Brown, D.; Campbell-Brown, M.; Ceranna, L.; et al. A 500-kiloton airburst over Chelyabinsk and an enhanced hazard from small impactors. *Nature* **2013**, *503*, 238–241. [CrossRef]
86. Silber, E.A.; ReVelle, D.O.; Brown, P.G.; Edwards, W.N. An estimate of the terrestrial influx of large meteoroids from infrasonic measurements. *J. Geophys. Res. Planet* **2009**, *114*, E08006. [CrossRef]
87. De Carlo, M.; Ardhuin, F.; Le Pichon, A. Atmospheric infrasound generation by ocean waves in finite depth: Unified theory and application to radiation patterns. *Geophys. J. Int.* **2020**, *221*, 569–585. [CrossRef]
88. De Carlo, M.; Hupe, P.; Le Pichon, A.; Ceranna, L.; Ardhuin, F. Global microbarom patterns: A first confirmation of the theory for source and propagation. *Geophys. Res. Lett.* **2021**, *48*, e2020GL09016. [CrossRef]
89. Abdullah, A.J. The musical sound emitted by a tornado. *Mon. Weather Rev.* **1966**, *94*, 213–220. [CrossRef]
90. Schecter, D.A. A brief critique of a theory used to interpret the infrasound of tornadic thunderstorms. *Mon. Weather Rev.* **2012**, *140*, 2080–2089. [CrossRef]
91. Akhalkatsi, M.; Gogoberidze, G. Infrasound generation by tornadic supercell storms. *Q. J. R. Meteor. Soc.* **2009**, *135*, 935–940. [CrossRef]
92. Akhalkatsi, M.; Gogoberidze, G. Spectrum of infrasound radiation from supercell storms. *Q. J. R. Meteor. Soc.* **2011**, *137*, 229–235. [CrossRef]

93. Ash, R.L.; Zardadkhan, I.; Zuckerwar, A.J. The influence of pressure relaxation on the structure of an axial vortex. *Phys. Fluids* **2011**, *23*, 073101. [CrossRef]
94. Ash, R.L.; Zardadkhan, I.R. Non-equilibrium behavior of large-scale axial vortex cores. *AIP Adv.* **2021**, *11*, 025320. [CrossRef]